Effects of substitution on the exchange stiffness and magnetization of Co films

C. Eyrich,[1] A. Zamani,[1,2] W. Huttema,[1] M. Arora,[1] D. Harrison,[1] F. Rashidi,[1] D. Broun,[1] B. Heinrich,[1] O. Mryasov,[3] M. Ahlberg,[2] O. Karis,[2] P. E. Jönsson,[2] M. From,[4] X. Zhu,[5] and E. Girt[1,*]

[1]*Simon Fraser University, 8888 University Drive, Burnaby, British Columbia V5A 1S6, Canada*

[2]*Uppsala University, P.O. Box 256, SE-751 05 Uppsala, Sweden*

[3]*University of Alabama, Tuscaloosa, Alabama 35487, USA*

[4]*Western Washington University, 516 High Street, Bellingham, Washington 98225, USA*

[5]*Seagate Technology, Fremont, California 94538 USA*

(Received 31 October 2013; revised manuscript received 21 August 2014; published 3 December 2014)

An antiferromagnetically coupled FM/NM/FM (FM = ferromagnet, NM = normal metal) trilayer structure responds to an external magnetic field by the formation of a magnetic-moment spring within the FM layers. We show that the exchange stiffness (A_{ex}) of an FM layer can be determined by fitting the field-dependent magnetization, $M(H)$, of the FM/NM/FM trilayer to a micromagnetic model. Using this method, we have measured the exchange stiffness of thin-film Co alloyed with Cr, Fe, Ni, Pd, Pt, and Ru. The results show that the rate at which a substituent element reduces the exchange stiffness is not directly related to its effect on the magnetization of the alloy. The observed trends have been understood by material-specific modeling based on density functional theory within the local density approximation. The stiffness measurements are in agreement with Brillouin light scattering carried out on thicker Co films.

DOI: 10.1103/PhysRevB.90.235408 PACS number(s): 75.70.Cn, 75.78.Cd, 75.30.Et

I. INTRODUCTION

In ferromagnetic materials there is competition between exchange energy, which favors uniform magnetization, and magnetostatic energy, which favors nonuniform magnetization. Since the exchange energy is short-ranged and the magnetostatic energy is long-ranged, the balance between these terms results in a characteristic length scale, the exchange length $\ell_{ex} = \sqrt{A_{ex}/\mu_0 M_s^2}$. Here A_{ex} is the exchange stiffness and M_s is the saturation magnetization. A consequence of this is that uniform magnetization reversal can only be assumed for structures smaller than ℓ_{ex}, typically in the range 2 to 5 nanometers [1]. On larger length scales, and even for materials smaller than ℓ_{ex} in which the intrinsic magnetic properties vary spatially, magnetization reversal is in general nonuniform. In these cases A_{ex} must be known in order to predict and control magnetization behavior. In applications such as magnetic recording media A_{ex} is one of the key parameters controlling nonuniform magnetization reversal [2–4].

In addition to the exchange and magnetostatic energies, the total free magnetic energy also includes terms for anisotropy, thermal, and Zeeman energies, which depend on M_s and an anisotropy constant, K. While M_s and K are readily accessible (from magnetization loops and torque measurements, respectively) it is not a trivial matter to measure A_{ex}.

To date, the most common way to determine A_{ex} is through a measurement of the dispersion curve of the spin waves. This can be done using Brillouin light scattering (BLS) [5–8], inelastic neutron scattering (NS) [9–11], or ferromagnetic resonance (FMR) [12–15]. The exchange stiffness is particularly difficult to measure in thin magnetic films, as the energy required to excite bulk magnons is inversely proportional to the square of the film thickness [5]. To illustrate how serious a problem this is, the first-order magnon mode in a 10-nm-thick cobalt film has a frequency of approximately 500 GHz (calculated in zero applied field assuming $A_{ex} = 1.55 \times 10^{-6}$ erg/cm, $M_s = 1247$ emu/cm^3 (measured in Co films investigated in this study), and an electron g factor of 2.16 [5]). This frequency is not accessible with FMR. In thin magnetic films, neutron scattering measurements can only be carried out in reflectivity mode due to the large penetration depth of neutrons. For these reasons, the spin-wave-dispersion methods of determining exchange stiffness is typically limited to films exceeding 30 nm in thickness.

An alternative method for measuring A_{ex} is by inducing nonuniform reversal in magnetic materials. Scholl *et al.* have shown that a ferromagnetic/antiferromagnetic structure responds to an external field by the creation of an exchange spring: the ferromagnetic layer rotates toward the field direction and creates a planar domain wall in the exchange-coupled antiferromagnetic layer [16]. By using x-ray magnetic linear dichroism spectroscopy, the rotation of magnetic moments in the antiferromagnetic layer can be detected and the exchange stiffness of the antiferromagnet inferred.

In this paper we employ a method for measuring A_{ex} that also relies on the creation of an exchange spring, the difference being that the planar domain walls are formed in ferromagnetic layers [17,18]. We investigate a FM/NM/FM film structure in which two ferromagnetic layers (FM) are antiferromagnetically coupled via the Ruderman-Kittel-Kasuya-Yosida (RKKY) interaction across a normal metal (NM) spacer layer. In the presence of an external field, the reversal in this structure is nonuniform, with the formation of an exchange spring in each FM.

There is significant interest in doped hexagonal-close-packed (hcp) Co materials because of their use as recording layers in hard drives. hcp Co is the only 3*d* ferromagnet with lower than cubic symmetry. It therefore has a much larger magnetocrystalline anisotropy energy than other 3*d* ferromagnets, such as Ni and Fe. The magnetocrystalline anisotropy of Co can be further increased through the addition of Pt, making it even more attractive for recording applications.

*egirt@sfu.ca

These high-anisotropy Co alloys can be fabricated at room temperature, simplifying the manufacturing process.

In this work we have studied a series of doped Co thin films with composition $Co_{100-\delta}X_\delta$, where $X =$ Cr, Fe, Ni, Pd, Ru, and Pt, and $\delta \leqslant 20$. To maximize the antiferromagnetic coupling between the FM layers, we have selected Ru as the NM spacer. For the majority of the CoX films, when $\delta \leqslant 12$ the coupling across the Ru layer is above 2 erg/cm^2.

II. THEORY

The theory of exchange interactions in 3d-metal-based magnets is an extremely challenging problem due to the strong hybridization between relatively localized d states and delocalized s and p states. Thus for a quantitative description of exchange coupling, both localized and delocalized moments play important roles. In the general case, the itinerant character of magnetism in these materials leads to uncertainty in the properties of the effective spin-interaction Hamiltonian. This means that both the *a priori* extent of significant interactions and the *a priori* importance of contributions beyond the Heisenberg model are unknown [19].

The concept of an effective Heisenberg exchange interaction has recently been defined within density functional perturbation theory with a more detailed description of the electronic states (a full spd basis set) for the selected spin configuration (normally the ground state) [20]. This approach has been successfully tested on 3d transition metals in their cubic phase [19] and for transition-metal-based intermetallics such as $L1_0$ FePt [21,22].

The situation in hcp Co has been given insufficient attention, especially the effect of 3d, 4d, and 5d substitutions. Here we use a first-principles approach to investigate the effect of finite thickness (the ultrathin-film limit) and the dependence on composition in CoX thin-film alloys. We use the Heisenberg exchange energy, given in the classical approximation by

$$E_{\rm ex} = \sum_{i \neq j} J_{ij}(1 - \vec{e}_i \cdot \vec{e}_j), \tag{1}$$

to calculate energy of planar spin wave given by magnetization distribution $\vec{e}_i(\vec{q}_i) = (\cos(\vec{q}\vec{r}_i), \sin(\vec{q}\vec{r}_i), 0)$ [23]. Here J_{ij} are the exchange interaction constants, and $\vec{e}_i = \frac{\vec{m}_i}{|m_i|}$ and $\vec{e}_j = \frac{\vec{m}_j}{|m_j|}$ are unit vectors of atomic magnetic moment $\vec{m}_i$ and $\vec{m}_j$ on the lattice sites i and j. In the limit of the long-wavelength approximation Eq. (1) can be expressed as $E_{\rm ex} = A_{ex} V q^2$, where V is unit cell volume. In our experiment and calculations the spin spiral vave vector q is along the [0001] direction of CoX hcp structure.

The dependence of $A_{\rm ex}$ on dopant content δ can be expressed as

$$A_{\rm ex}(\delta) \approx A_{\rm ex}(0)\left[1 - \frac{1}{N_s}\sum_{s=0}^{N_s}\frac{\Delta J_0^{(s)}(\delta)}{J_0}\right], \tag{2}$$

where the stiffness of an element without dopants is $A_{\rm ex}(0)$, and the change in the molecular field exchange constant in individual shells with doping is given by $\Delta J_0^{(s)}(\delta) = J_0 - J_0^{(s)}(\delta)$. N_s is the number of nearest-neighbor shells affected by the presence of foreign atoms. The molecular field exchange constant for atom "0", belonging to the shell "s", $J_0^{(s)}(\delta) = \sum_j J_{0j}(\delta)$, is defined as the sum over all significant neighbors (index j), and J_0 is the exchange constant for the pure material (hcp Co). The calculations are done in the dilute limit where the exchange coupling between the dopant atoms is negligible.

The microscopic origin of variations of the exchange coupling constant due to dopant atoms can be understood using a picture of atomic magnetic moments $(\vec{m}_i, \vec{m}_j)$ on sites i, j, and overlapping wave functions. This picture leads to the notion of a response function, $R_{ij}(\delta)$, as a function of dopant concentration, contributing to the overall exchange coupling constant between sites i and j [20,24], which can be used to express the exchange interaction constants J_{ij} as

$$J_{ij} \approx \Delta_i R_{ij}(\delta)\Delta_j. \tag{3}$$

Here Δ_i and Δ_j are exchange splittings on sites i and j, respectively, and are given within the Stoner model by a product of a so-called Stoner intra-atomic exchange parameter, I, and the atomic magnetic moment: $\Delta_i = I_i m_i$ and $\Delta_j = I_j m_j$. Thus, according to this general description, 3, dopant atoms will alter the exchange coupling constants via two major mechanisms: (i) variation of atomic magnetic moment and (ii) variation of response function.

To understand in detail how both mechanisms contribute to J_{ij} in the presence of foreign atoms, we have performed density functional calculations of exchange coupling constants using a multiple-scattering-theory solution of the two-impurity model [20] implemented within the linear muffin-tin orbital method within the atomic sphere (LMTO-ASA) [19,24].

As an alternative, we have also performed constrained density functional calculations (CLSDA) [24] for spin-spiral magnetic structures within the LMTO-ASA method [24]. The CLSDA total-energy calculations of noncollinear spin configurations [24] are a convenient way of determining the exchange coupling constants (molecular field constants) for the dopant atoms and for the host atomic moments located in the shells neighboring the dopant atoms. In these calculations we have neglected short-range fluctuations and assumed that the distance between two dopants is given by the average value calculated from the dopant concentration.

The M_s values for different dopant contents are calculated using a supercell geometry. The atomic spin moments for dopant and neighboring Co shells are calculated from

$$m_i = \int_{-\infty}^{\epsilon_F} [n_i^{\uparrow}(\epsilon) - n_i^{\downarrow}(\epsilon)]d\epsilon, \tag{4}$$

where $n_i^{\uparrow}$ and $n_i^{\downarrow}$ are the projected density of states for majority and minority spins at site i and ϵ_F is the Fermi level.

III. EXPERIMENT

The magnetic films were deposited at room temperature onto Si (100) substrates using direct-current and radio-frequency sputtering techniques. Prior to the deposition, the substrates were cleaned in hexane and methanol baths heated to 50 °C to remove organics from the surface, and then rinsed in deionized water. All three processes were aided by ultrasonic agitation. Upon removal from deionized water the wafers were blown dry with N_2 gas.

The base pressure in the deposition chamber was about 5×10^{-8} Torr. The Ar gas pressure was kept as low as possible during deposition to obtain smoother films [25]. In most of the films, deposition of CrTa, Ta, Pt, and Cu was at 1.7 mTorr, while the magnetic CoX and Ru layers were deposited at 2.2 mTorr. The films consisted of a CrTa(30 nm)/Pt(10 nm), CrTa(30 nm)/Cu(10 nm), or Ta(3 nm)/Cu(10 nm) seed layer followed by Ru(4 nm)/$Co_{100-\delta}X_\delta(t_1)$/Ru($t_2$)/$Co_{100-\delta}X_\delta(t_1)$/Ru(4 nm). Here X = Cr, Fe, Ni, Ru, Pd, and Pt, and δ was varied from 0 to 20. In the case of $Co_{100-\delta}Ru_\delta$ ($\delta = 15$ and 20) we also deposited a 1-nm-thick Co interface layer on both sides of Ru(t_2) in order to increase RKKY coupling strength [26,27]. To maximize the antiferromagnetic coupling between CoX layers, the Ru spacer layer thickness, t_2, was kept between 0.38 and 0.45 nm. To measure the saturation magnetization of bulk Co we deposited a thick Co film surrounded with thin Ru layers, Ru(3 nm)/Co(80 nm)/Ru(3 nm).

The film thickness was obtained from the slope of $m\lambda/2$ as a function of $\sqrt{\sin^2(\phi_m) - \sin^2(\phi_c)}$, where $\lambda = 0.15418$ nm is the wavelength of the Cu $K\alpha$ x rays and m and ϕ_m are the Bragg order and the angle of low-angle x-ray diffraction, respectively. ϕ_c is the critical angle for total reflection. Our films were smooth enough to detect very high order reflections. This allowed for the very accurate thickness measurements that are critical for determining M_s.

X-ray measurements also confirmed that the orientation of the Pt, Cu, Ru, and Co layers were unaffected by the choice of CrTa or Ta as a seed layer. Cu and Pt crystallize in a face-centered-cubic (fcc) crystal structure and grow along the ⟨111⟩ directions on top of CrTa or Ta. Co and Ru layers crystallize in a hcp crystal structure and grow epitaxially on top of Cu or Pt grains along the [0001] direction. The full width at half maximum of the c-axis distribution of CoX and Ru layers, grown on top of dual (CrTa or Ta)/(Pt or Cu) seed layers, was around 3°. 80 nm Co films grown on top of a single Ta seed layer were only weakly textured.

Magnetization curves were measured using both a vibrating sample magnetometer (VSM) and superconducting quantum interference device (SQUID) magnetometer. The uniaxial anisotropy, K_u, of hcp CoX films was determined from torque measurements of (0001) textured Ta(3 nm)/Ru(4 nm)/CoX(10 nm)/Ru(4 nm) structures, at room temperature. The Curie temperature, T_c, of CoRu alloys was determined from the $M(T)$ measurements conducted on Ta(3 nm)/Ru(4 nm)/$Co_{100-\delta}Ru_\delta$ (40 nm)/Ru(4 nm) (δ = 11, 17, and 22) at temperatures below 1000 K in a physical properties measurement system (PPMS).

BLS data were collected in the backscattering geometry using the green line from an argon ion laser at an incident power of 100 mW at an incident angle of 45° to the sample normal on Ta(3 nm)/Co(80 nm)/Ta(3 nm). The light scattered by the sample was analyzed by a 4-pass scanning Fabry-Perot interferometer with a free spectral range of approximately 50 GHz.

IV. METHOD FOR DETERMINING A_{ex}

We consider the case of an FM/NM/FM trilayer structure, in which the two ferromagnetic layers are antiferromagnetically coupled across a nonmagnetic spacer layer.

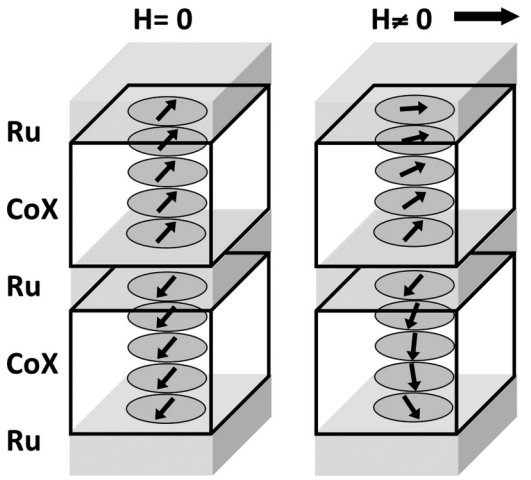

FIG. 1. Formation of the exchange spring in an antiferromagnetically coupled FM/NM/FM film structure when subjected to an external magnetic field as predicted by our micromagnetic model. We assume that the spins in each atomic plane rotate coherently.

In developing the micromagnetic model, the simulations are limited to the experimentally relevant situation in which the external magnetic field is applied parallel to the surface of the films and the magnetic moments lie in the plane during magnetization reversal. In the CoX films discussed in this paper, the demagnetization field, $4\pi M_s$, is larger than the anisotropy field perpendicular to the film plane, $2K_u/M_s$, resulting in an in-plane magnetization. Table I lists values of the effective magnetization $4\pi M_{\text{eff}} = 4\pi M_s - 2K_u/M_s$ for the Co and CoX films. Magnetic force microscopy (MFM) measurements confirm the in-plane orientation of the magnetization of [0001]-textured Co films with thickness less than 30 nm [36].

We make an additional assumption in the model: that that there is no *in-plane* magnetocrystalline anisotropy in the FM layers. This is well justified, since the CoX films used in this study were polycrystalline and the substrates were rotated during deposition, resulting in no significant in-plane variation.

Provided the investigated film structures are uniform perpendicular to the film's growth direction, the magnetization reversal in these structures can be described by a one-dimensional micromagnetic model. In this model, each FM layer consists of N magnetic atomic planes that interact only with their nearest vertical neighbors through the direct exchange interaction. We assume that the magnetic moments in each atomic plane rotate coherently. In the model, the atomic planes were separated by $d = 0.204$ nm, which is the distance between neighboring Co atomic planes along the [0001] direction. In this case and in the presence of an external magnetic field, competition between the Zeeman, RKKY, and exchange energies creates a spin spiral in each FM layer, as shown in Fig. 1.

The direction of the magnetic moments in each magnetic atomic plane in the FM layers as a function of the strength of the external magnetic field is then calculated by minimizing the total magnetic energy per unit area. The total magnetic

TABLE I. $M_s(\mathrm{Co}) = 1247 \pm 37$ emu/cm^3 and $A_{\mathrm{ex}}(\mathrm{Co}) = 1.55 \pm 0.09 \times 10^{-6}$ erg/cm are average values obtained from 5 different Co(t_1)/Ru/Co(t_1) (10 nm $\leqslant t_1 \leqslant$ 10.8 nm). M_s for bulk Co is 1440 emu/cm^3 [1]. The largest $J_{\mathrm{RKKY}}(\mathrm{Co}) = 4.20 \pm 0.13$ erg/cm^2 is measured in Co/Ru(0.38 nm)/Co structures. K_u is uniaxial anisotropy of hcp CoX(10 nm) in (0001) textured Ru/CoX/Ru films. K_u of 10 nm Co films is two times lower than K_u of bulk Co due to the presence of stacking faults [35]. $4\pi M_{\mathrm{eff}} = 4\pi M_s - 2\frac{K_u}{M_s}$, and $^{(\alpha)}$ and $^{(\epsilon)}$ are T_c values of α-(Co) (fcc Co) and ϵ-(Co) (hcp Co), respectively. $^{(\bullet)}$ indicates that $M(H)$ measurements were performed at 10 K, and $^{(*)}$ indicates the presence of 1 nm Co interface layer between CoRu and Ru spacer layers.

	δ	M_s(CoX) (emu/cm^3)	$\frac{M_s(\mathrm{Co}X)}{M_s(\mathrm{Co})}$	A_{ex}(CoX) (10^{-6} erg/cm)	$\frac{A_{\mathrm{ex}}(\mathrm{Co}X)}{A_{\mathrm{ex}}(\mathrm{Co})}$	J_{RKKY}(CoX) (erg/cm^2)	$\frac{J_{\mathrm{RKKY}}(\mathrm{Co}X)}{J_{\mathrm{RKKY}}(\mathrm{Co})}$	K_u(CoX) (10^6 erg/cm^3)	$4\pi M_{\mathrm{eff}}$ (kOe)	T_c (K)
Co	0	1247 ± 37	1.00	1.55 ± 0.09	1.00	4.20 ± 0.13	1.00	2.1 ± 0.3	12.29	1360$^{(\epsilon)}$ [1] 1400$^{(\alpha)}$ [28]
	3	1110 ± 37	0.89	1.30 ± 0.09	0.84	3.19 ± 0.13	0.76	3.5 ± 0.3	7.64	1280$^{(\alpha)}$ [29]
Co$_{100-\delta}$Cr$_\delta$	6	960 ± 37	0.77	1.16 ± 0.09	0.75	2.10 ± 0.13	0.50	4.3 ± 0.3	3.10	1180$^{(\epsilon)}$ [29]
	12	715 ± 37	0.57	0.90 ± 0.09	0.58	0.90 ± 0.13	0.26	3.2 ± 0.3	1.00	940$^{(\epsilon)}$ [29]
Co$_{100-\delta}$Fe$_\delta$	10	1347 ± 37	1.08	1.55 ± 0.09	1.00	4.20 ± 0.13	1.00			1320$^{(\alpha)}$ [30]
	20	1447 ± 37	1.16	1.55 ± 0.09	1.00	4.96 ± 0.13	1.18			1210$^{(\alpha)}$ [30]
Co$_{100-\delta}$Ni$_\delta$	8	1222 ± 37	0.98	1.29 ± 0.09	0.83	3.61 ± 0.13	0.86			1360$^{(\alpha)}$ [28]
	16	1160 ± 37	0.93	1.12 ± 0.09	0.72	2.94 ± 0.13	0.70			1320$^{(\alpha)}$ [28]
Co$_{100-\delta}$Ru$_\delta$	2	1235 ± 37	0.99	1.36 ± 0.09	0.88	3.61 ± 0.13	0.86			1340$^{(\alpha)}$ [31]
	4	1160 ± 37	0.93	1.21 ± 0.09	0.78	3.19 ± 0.13	0.76			1250$^{(\alpha)}$ [31]
	6	1097 ± 37	0.88	1.05 ± 0.09	0.68	2.52 ± 0.13	0.60			1170$^{(\alpha)}$ [31]
	8	985 ± 37	0.79	0.85 ± 0.09	0.55	2.10 ± 0.13	0.50			1050$^{(\alpha)}$ [31]
	10	927 ± 37	0.74	0.74 ± 0.09	0.48	1.60 ± 0.13	0.38	3.0 [32]	5.17	820$^{(\alpha)}$ [31]
		973 ± 37$^{(\bullet)}$	0.78	0.78 ± 0.09$^{(\bullet)}$	0.50	1.68 ± 0.13$^{(\bullet)}$	0.40			1100$^{(\epsilon)}$ [31]
	11									1035$^{(\epsilon)}$
	12	860 ± 37	0.69	0.60 ± 0.09	0.39	1.22 ± 0.13	0.29			1060$^{(\epsilon)}$ [31]
	15	723 ± 62	0.58	0.48 ± 0.12	0.31	3.30 ± 0.13$^{(*)}$	0.78			970$^{(\epsilon)}$ [31]
	17									795$^{(\epsilon)}$
	20	536 ± 62	0.43	0.26 ± 0.12	0.17	3.01 ± 0.13$^{(*)}$	0.72			800$^{(\epsilon)}$ [31]
		673 ± 37$^{(\bullet)}$	0.54	0.33 ± 0.09$^{(\bullet)}$	0.21	3.40 ± 0.13$^{(*\bullet)}$	0.81			
	22									530$^{(\epsilon)}$
Co$_{100-\delta}$Pd$_\delta$	9	1097 ± 37	0.88	1.26 ± 0.09	0.81	3.32 ± 0.13	0.79			1360$^{(\alpha)}$ [33]
	17	1060 ± 37	0.85	0.99 ± 0.09	0.64	2.56 ± 0.13	0.61			1290$^{(\alpha)}$ [33]
Co$_{100-\delta}$Pt$_\delta$	3	1210 ± 37	0.97	1.41 ± 0.09	0.91	3.70 ± 0.13	0.88	3.2 ± 0.3	9.91	1390$^{(\alpha)}$ [34]
	6	1210 ± 37	0.94	1.41 ± 0.09	0.91	3.49 ± 0.13	0.83	4.3 ± 0.3	8.09	1380$^{(\alpha)}$ [34]
	9	1085 ± 37	0.87	1.41 ± 0.09	0.91	2.98 ± 0.13	0.71	5.4 ± 0.3	3.67	1360$^{(\alpha)}$ [34]
	12	1097 ± 37	0.88	1.30 ± 0.09	0.84	2.52 ± 0.13	0.60	6.5 ± 0.3	1.93	1340$^{(\alpha)}$ [34]

energy of the system, E_{mag}, can be written as

$$E_{\mathrm{mag}} = E_{\mathrm{RKKY}} - E_{\mathrm{ex}} - E_Z,$$

$$E_{\mathrm{RKKY}} = J_{\mathrm{RKKY}} \cos(\theta_N - \theta_{N+1}),$$

$$E_{\mathrm{ex}} = \frac{2A_{\mathrm{ex}}}{d}\left[\sum_{i=1}^{N-1} \cos(\theta_i - \theta_{i+1}) + \sum_{i=N+1}^{2N-1} \cos(\theta_i - \theta_{i+1})\right],$$

$$E_Z = M_s H d \sum_{i=1}^{2N} \cos(\theta_i). \quad (5)$$

We will call this the *single-layer model*, because we assume that there is no variation in the local values of M_s and A_{ex} across the FM layers. In the model we also assume that the bilinear RKKY coupling acts solely between the ferromagnetic atomic planes bordering the nonmagnetic spacer layer. For this reason, E_{RKKY} depends only on the angle between the magnetization directions of the atomic planes θ_N and θ_{N+1}, and the exchange coupling constant J_{RKKY}. E_{ex}, in Eq. 5, represents the energy contribution from the direct exchange interaction between nearest-neighbor atomic planes within each magnetic layer. θ_i is the angle of the magnetic moments in each magnetic atomic plane i with respect to the direction of the applied magnetic field, H. E_Z is the Zeeman energy due to the interaction between the applied magnetic field and the magnetic moments in each atomic plane.

To calculate $M(H)$ we first have to determine the magnetization angle of each atomic plane within the FM layers as a function of H. This was carried out by minimizing E_{mag} with respect to the set of θ_i, i.e., by setting $\frac{\partial E_{\mathrm{mag}}}{\partial \theta_i} = 0$. We compare the model to a normalized $M(H)$ curve; therefore, for a given field H, the total magnetization of the FM/NM/FM structure along the direction of the applied field is

$$M(H) = \frac{1}{2N} \sum_{i=1}^{2N} \cos(\theta_i). \quad (6)$$

For the purposes of fitting to the experimental data, the saturation magnetization of the FM/NM/FM structure was determined by high field magnetization measurements and

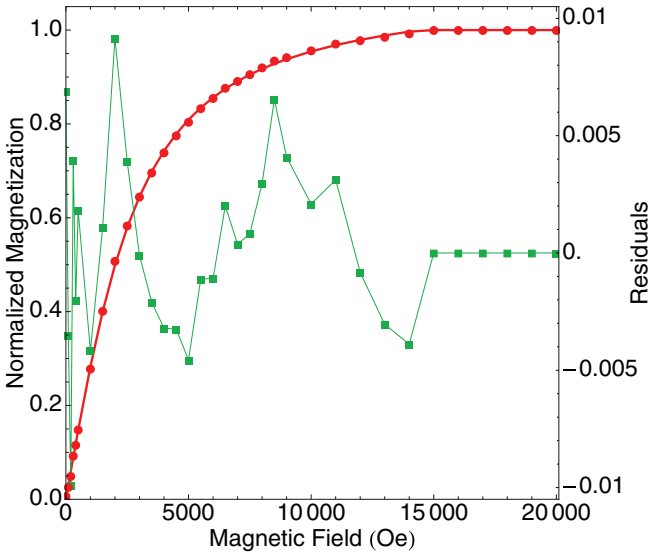

FIG. 2. (Color online) Measured and fitted $M(H)$ curves of Co(10 nm)/Ru/Co(10 nm). Fitting was done using the single-layer micromagnetic model. The filled circles are the measured values, the solid line that passes through the solid circles is the fitted curve, and the filled squares are the residuals from the fit.

was therefore not a fitting parameter. A_{ex} and J_{RKKY}, the only free parameters in the model, were determined by minimizing the difference between the calculated $M(H)$ and the measured data, $M_{expt}(H)$, using a least-squares method [37]. Figure 2 shows both the calculated and measured $M(H)$ curves for Co/Ru/Co and the difference (residuals) between the two sets of data. A χ^2 plot for Co(10 nm)/Ru/Co(10 nm) with 1σ, 2σ, and 3σ confidence intervals in A_{ex} and J_{RKKY} is shown in Fig. 3.

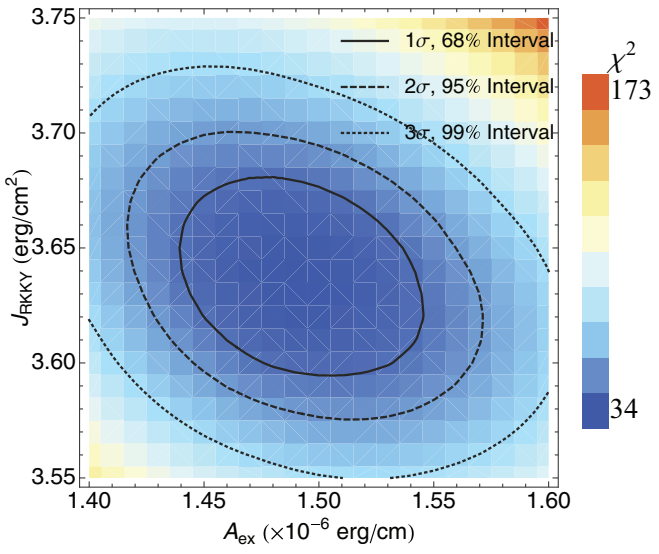

FIG. 3. (Color online) χ^2 values from fitting the $M(H)$ dependence of Co(10 nm)/Ru/Co(10 nm) for a grid of A_{ex} and J_{RKKY} values around the initial estimate. The minimum χ^2 value occurs for $A_{ex} = 1.49 \times 10^{-6}$ erg/cm and $J_{RKKY} = 3.64$ erg/cm^2. The solid line encircles the 1σ confidence interval, the dashed line the 2σ interval, and dotted line the 3σ interval [37].

TABLE II. Results of fitting the $M(H)$ data of Co(10 nm)/Ru(0.38 nm)/Co(10 nm) to the triple-layer model. The triple-layer model is not sensitive to changes in $A_{ex\,ext}$, as reducing this value by a factor of 6 from 1.49×10^{-6} erg/cm to 0.25×10^{-6} erg/cm had no measurable effect on $A_{ex\,bulk}$ and χ^2. The best fit is obtained using $A_{ex\,int} = 1.48 \times 10^{-6}$ erg/cm and $A_{ex\,ext} = 1.52 \times 10^{-6}$ erg/cm. The 1σ bound on $A_{ex\,int}$ and $A_{ex\,bulk}$ is at 1.1×10^{-6} erg/cm and 1.79×10^{-6} erg/cm, respectively.

$M_{s\,int}$, $M_{s\,ext}$ ($\frac{emu}{cm^3}$)	$M_{s\,bulk}$ ($\frac{emu}{cm^3}$)	$A_{ex\,int}$	$A_{ex\,bulk}$ (10^{-6} $\frac{erg}{cm}$)	$A_{ex\,ext}$	J_{RKKY} ($\frac{erg}{cm^2}$)	χ^2
1247	1247	1.49	1.49	1.49	3.64	30.3
1080	1300	1.48	1.52	1.49	3.64	30.2
1080	1300	1.48	1.52	0.25	3.64	30.7
1080	1300	1.10	1.79	1.49	3.64	40.9

A more accurate micromagnetic model must allow for the possibility that both M_s and A_{ex} differ from their bulk values in the vicinity of the FM(CoX)/NM(Ru) interfaces. For this reason, we have developed a so-called *triple-layer model*. Each FM layer is divided into three regions: (1) exterior interfaces, the FM atomic planes that border the seed and capping Ru layers; (2) bulk material; and (3) interior interfaces, the FM atomic planes that border the Ru spacer layer. The exchange stiffnesses $A_{ex\,ext}$, $A_{ex\,bulk}$, and $A_{ex\,int}$ describe the direct exchange interaction between atomic planes in the exterior interface, bulk, and interior interface layers, respectively. Between the interface and bulk atomic planes we assume that A_{ex} is equal to the average of the two exchange stiffnesses.

The FM film consists of N layers atomic planes, while the exterior and interior interfaces extend for K and L atomic planes, respectively. The saturation magnetization of the bulk layer is calculated using $M_{s\,bulk} = (N \times M_{s\,tot} - K \times M_{s\,ext} - L \times M_{s\,int})/(N - K - L)$ (used in Table II). The different M_s were not fitted; instead we have assumed that the $M_{s\,int}$ and $M_{s\,ext}$ of the 1.2-nm-thick internal and external interfaces are equal to 1080 emu/cm^3, which is the M_s of the 2.4 nm Co layer in the Ru/Co(2.4 nm)/Ru/Co(2.4 nm)/Ru structure.

V. EXCHANGE STIFFNESS AND MAGNETIZATION SATURATION OF CoX

A. A_{ex} versus thickness measurement in Co

We used the single-layer model to fit measured $M(H)$ data obtained for Co(t_1)/Ru/Co(t_1), where t_1 ranged from 2.4 nm to 20 nm. Figure 4 shows the dependence of M_s and A_{ex} on t_1 in Co/Ru/Co. The error bars were estimated from 5 different Co(t_1)/Ru/Co(t_1) (10 nm $\leqslant t_1 \leqslant$ 10.8 nm) structures for which fittings using the single-layer model give $A_{ex} = 1.55 \pm 0.09 \times 10^{-6}$ erg/cm and $M_s = 1247 \pm 37$ emu/cm^3. We observe a very weak increase of M_s if $t_1 \geqslant 3$ nm, as shown in Fig. 4(a). This is evident from magnetization measurements on a Ru/Co/Ru structure consisting of an 80-nm-thick single Co layer surrounded by Ru seed and capping layers, for which $M_s = 1350$ emu/cm^3. The structures with a thick Co film were prepared only to justify our claim and are included in Fig. 4(a). For $t_1 < 3$ nm the decrease in M_s is much more pronounced.

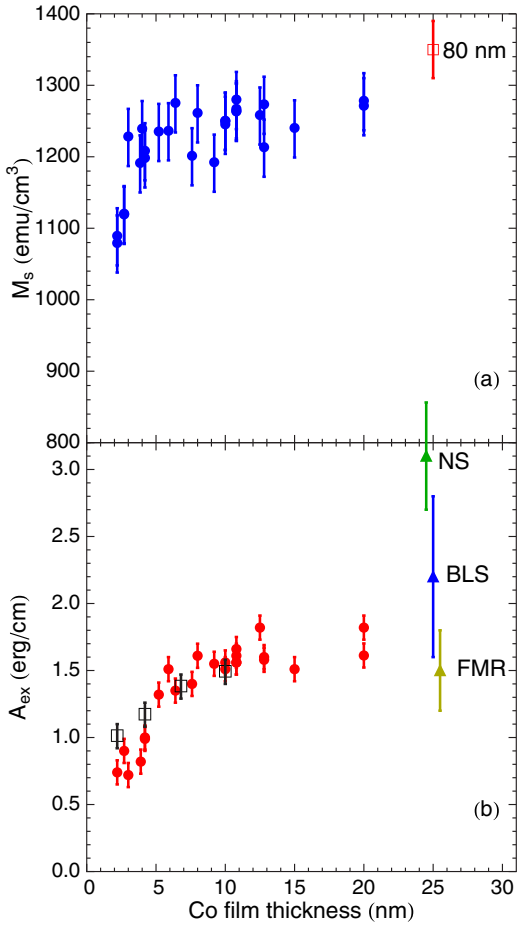

FIG. 4. (Color online) M_s (top figure) and A_{ex} (bottom figure) of the Co films in the Ta/Cu/Ru/Co(t_1)/Ru/Co(t_1)/Ru structures as a function of the Co film thickness, t_1, obtained using the single-layer model. The top figure includes M_s of bulk Co ($M_s = 1350$ emu/cm^3) measured in 80-nm-thick single Co films. The bottom figure also shows (the squares) A_{ex} values obtained by fitting including biquadratic coupling in the single-layer model, as well as neutron scattering (NS) [9–11], Brillouin light scattering (BLS) [5,8], and ferromagnetic resonance (FMR) [12,14] data of A_{ex} of Co reported by other groups.

A_{ex} increases with Co thickness: the increase is steep for $t_1 < 6$ nm, and gradual for thicker Co layers, as shown in Fig. 4(b). For the thinnest films there might be an additional biquadratic coupling term, $J_2 \cos^2(\theta_N - \theta_{N+1})$, that has to be added to the micromagnetic model. J_2 has a $1/t_1^2$ dependence, assuming that the roughness of the Co films is independent of the Co film thickness. Therefore, it is expected that this term only plays a significant role in describing the coupling between ultrathin magnetic films. This was confirmed by adding biquadratic coupling to Eq. (5) and calculating A_{ex} as a function of thickness. We found that by including biquadratic coupling, the decrease in A_{ex} with t_1 is less pronounced, and that for $t_1 > 6$ nm the best fit has $J_2 = 0$.

From Fig. 4(b) it is also evident that for $t_1 > 6$ nm, the values of A_{ex} obtained with the micromagnetic calculations are in agreement with FMR measurements [12,14] of thick Co films but are smaller than A_{ex} inferred using NS [9–11] and BLS [5,8].

To avoid Co thickness effects, measurements of A_{ex} and M_s of CoX films were done in CoX(10 nm)/Ru/CoX(10 nm) film structures. The observed reduction of A_{ex} and M_s is due to the interaction of Co films with nonmagnetic Ru interfaces.

In order to investigate the influence of this interaction on the determined A_{ex} and J_{RKKY}, we fitted the magnetization data of the Co(10 nm)/Ru/Co(10 nm) structure with the triple-layer model and compared it to the results of the single-layer model, which are presented in Fig. 2 and Fig. 3. The outcome of the triple-layer model fit is summarized in Table II. Since the RKKY coupling acts solely between the Co atomic planes bordering the Ru spacer layer any change in $A_{ex\,int}$ affects the reversal of a whole 10 nm Co film, while a change of $A_{ex\,ext}$ affects only the reversal of the 1.2 nm exterior interface layer. This explains why the the quality of the fit is almost insensitive to a change of $A_{ex\,ext}$ from 1.49×10^{-6} erg/cm to 0.25×10^{-6} erg/cm; see Table II. To minimize the number of fitting parameters, we have set $A_{ex\,ext} = 1.49 \times 10^{-6}$ erg/cm and studied how $A_{ex\,int}$, $A_{ex\,bulk}$, and J_{RKKY} affect the fitting. The best fit was obtained for $A_{ex\,int} = 1.48 \times 10^{-6}$ erg/cm, $A_{ex\,bulk} = 1.52 \times 10^{-6}$ erg/cm, and $J_{RKKY} = 3.64$ erg/cm^2 (Table II). Decreasing the strength of $A_{ex\,int}$ leads to an increase of $A_{ex\,bulk}$ as well as χ^2, but it stays within 1σ confidence for $A_{ex\,int} = 1.10 \times 10^{-6}$ erg/cm and $A_{ex\,bulk} = 1.79 \times 10^{-6}$ erg/cm.

Table II shows that the quality of the fit achieved with single layer and triple layer is the same. So, in order to minimize the number of free parameters, we decided to fit the $M(H)$ data of the CoX(10 nm)/Ru/CoX(10 nm) film structures using the single-layer model. The addition of more than 12 at. % of Ru significantly reduced the RKKY coupling between CoRu layers in the CoRu/Ru/CoRu structures. For this reason, a 1-nm-thick Co interface was deposited on both sides of the Ru spacer and A_{ex} of this structure was determined using the triple-layer model. As shown in Fig. 4 M_s and A_{ex} are reduced in thin Co films surrounded with Ru layers. For this reason in the fitting procedure we assumed three different A_{ex} and M_s values for the Co(1 nm) interface layers: that of pure Co; $Co_{94}Ru_6$; and $Co_{90}Ru_{10}$. The data presented for $Co_{100-\delta}Ru_\delta$ ($\delta = 15$ and 20) show the average values for both M_s and A_{ex} from these three fits and the error bars account for the variation in these results. These average values are practically identical to that of the 2.4 nm Co layer in the Ru/Co(2.4 nm)/Ru/Co(2.4 nm)/Ru structure presented in Fig. 4.

B. A_{ex} and M_s of CoX alloys

Figure 5 and Table III show the effect of alloying on M_s and A_{ex} of Co, obtained by fitting the single-layer model to the $M(H)$ dependence of CoX(10 nm)/Ru(t_2)/CoX(10 nm), where X = Cr, Fe, Ni, Ru, Pd, and Pt. All measured data are normalized to the corresponding quantities for pure Co, $A_{ex} = 1.55 \pm 0.09 \times 10^{-6}$ erg/cm and $M_s = 1247 \pm 37$ emu/cm^3. These values were obtained from 5 different Co(t_1)/Ru/Co(t_1) (10 nm $\leqslant t_1 \leqslant$ 10.8 nm) structures. For the majority of the CoX compositions, we deposited two film structures with the thickness of the Ru spacer layer, t_2, equal to 0.38 and 0.45 nm. The reported values are an average of the two measurements. From only two measurements the error bars cannot be accurately estimated. For this reason, for all data in

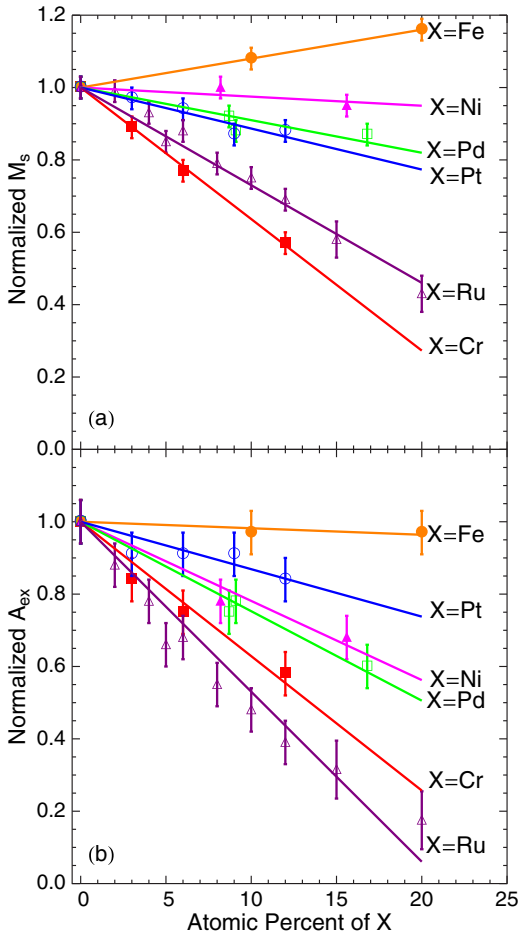

FIG. 5. (Color online) The effect of alloying on M_s and A_{ex} of Co. The M_s and A_{ex} values are normalized to that of Co films where $M_s = 1247$ emu/cm^3 and $A_{ex} = 1.55 \times 10^{-6}$ erg/cm. The lines through the points are only intended to help identify the trends in the M_s and A_{ex} data.

Fig. 5 we used the larger error bars of two: one obtained for pure Co layers, where we measured 5 different samples with the thickness between 10 nm and $\leqslant$ 10.8 nm, and a second obtained for CoX.

It is also evident from Table III and Fig. 5 that the rate of change of A_{ex} and M_s are not always correlated. Substitutions of Cr into Co reduce M_s the most while Ru additions have the largest effect on A_{ex}. Table III and Fig. 5 also show that, as

TABLE III. The effect of alloying on M_s and A_{ex} of Co, presented as the relative change per at. % of the dopant. The values correspond to the slope of the linear fits in Fig. 5 that pass through 1 for $\delta = 0$. The results differ from those published by Eyrich *et al.* [18] due to the procedure we used to calculate the slopes.

Dopant, X	$dM_s/d\delta$ (% per at. %)	$dA_{ex}/d\delta$ (% per at. %)
Cr	−3.6	−3.7
Ru	−2.7	−4.7
Pd	−1.0	−2.1
Pt	−1.0	−1.3
Ni	−0.4	−1.8
Fe	0.8	0

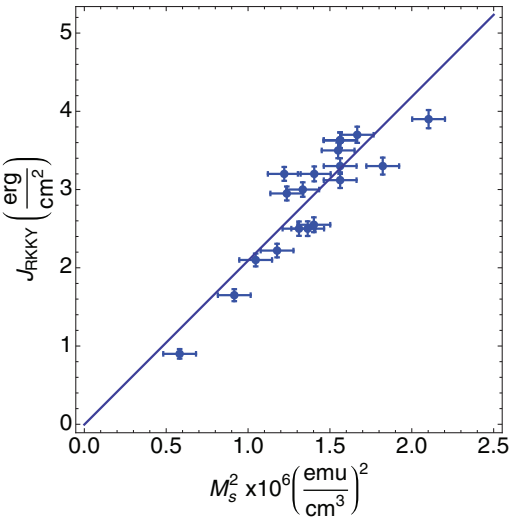

FIG. 6. (Color online) J_{RKKY} as a function of M_s^2 for all CoX alloys in CoX(10 nm)/Ru(0.38 nm)/CoX(10 nm) structures. The solid line is a linear fit through the experimental data.

expected, Fe increases M_s of Co. The two noble-metal alloys, Pt and Pd, have very similar effects on A_{ex} and M_s.

J_{RKKY} versus M_s^2 of CoX in CoX/Ru(0.38 nm)/CoX are shown in Fig. 6 together with a solid line representing a linear fit through the data. For a constant Ru spacer layer thickness, J_{RKKY} is linearly dependent on M_s^2, as predicted by the mean-field theory calculations [38].

C. Experiment versus DFT theory for CoX (X = Cr, Ru, and Pt)

The DFT calculations were performed for $Co_{100-\delta}X_\delta$, where X = Cr, Ru, and Pt, and $\delta = 0$, 2.78, 12.5. The calculations and experimental data are summarized in Fig. 7. From this figure, it is evident that the calculations match much better with the experimental values of M_s, shown in Fig. 7(a), than with the A_{ex} data, presented in Fig. 7(b). Despite this, the calculated values for A_{ex} confirm the trends observed from experiments. The DFT calculations were performed at 0 K while the experimental measurements were carried out at room temperature. For this reason we measured A_{ex} and M_s of $Co_{90}Ru_{10}$ and $Co_{80}Ru_{20}$ at 10 K (filled triangles, Fig. 7). From these plots it is clear that the low-temperature data are in better agreement with the DFT calculations suggesting that the discrepancy between the experimental and theoretical values could be in part due to temperature effects.

The effect that alloying has on M_s and A_{ex} can be explained from the results of the DFT calculations. The results of the DFT calculations are summarized in Table IV. To calculate the effects of alloying, a Co atom in a Co lattice was replaced by atom X; this atom is located at the 0 shell, $i = 0$. The magnetic moments and exchange coupling of the first three sets (shells) of nearest-neighbor Co atoms around the X atom are calculated before and after substituting an atom X for a Co atom. The nearest neighbors are in shell $i = 1$, the next nearest in shell $i = 2$, and so on. The exchange stiffness was calculated from the difference in magnetic energies before and after inducing a spin spiral to the moments in the Co lattice

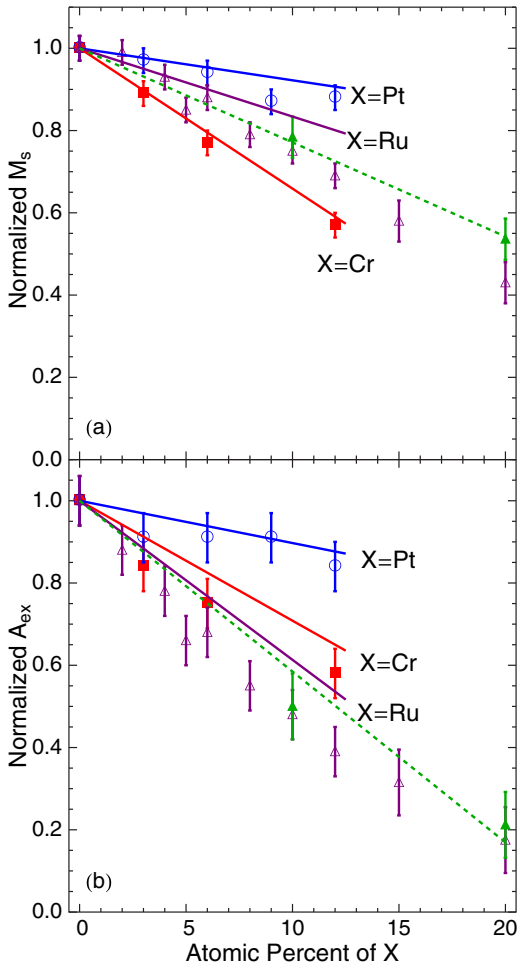

FIG. 7. (Color online) Experimental (circles) and DFT calculated (lines) values of (a) M_s, and (b) A_{ex} for CoRu, CoCr, and CoPt alloys. All M_s and A_{ex} data are measured at 298 K. M_s and A_{ex} of $Co_{90}Ru_{10}$ and $Co_{80}Ru_{20}$ were also measured at 10 K; these data are shown by the filled triangles and dashed lines.

perpendicular to the [0001] crystal direction. The spiral is similar to that which we assume is formed in CoX films of the CoX/Ru/CoX structure in the presence of applied magnetic field.

The DFT calculations, presented in Table IV, show that the magnetic moment of the substituted Cr atom is antiferromagnetically coupled to the Co neighbors and has a very large magnetic moment of $-2.2\ \mu_B$. The magnetic moment of substituted Pt and Ru atoms coupled ferromagnetically to the Co atoms. The induced magnetic moments in these atoms are $0.39\ \mu_B$ for Pt and $0.48\ \mu_B$ for Ru. The relative orientation of the Co, Cr, and Ru moments have been experimentally confirmed independently. The DFT results also show that the addition of Cr and Ru atoms reduces the magnetic moment of the surrounding Co atoms while the addition of Pt slightly increases the neighboring Co moments. The large antiferromagnetically coupled Cr moment combined with the reduction in the magnetic moments of Co atoms in CoCr alloys explains why the addition of Cr reduces M_s more than the other elements.

TABLE IV. The contributions of each shell to the magnetic moment and the exchange coupling are calculated in a Co lattice with and without an impurity atom X in the 0 shell. The nearest neighbors to the 0 shell are called the 1 shell and so on. m_0 magnetic moment of X atom in the shell 0, and m_1, m_2, and m_3 magnetic moments of Co atoms in the shells 1, 2, and 3, respectively. The $\Delta J_0^{(s)}$ is the change in the molecular field exchange constant in individual shells due to the presence of an X atom in shell 0, and $\Delta J_{av} = -\frac{1}{N_s}\sum_{s=0}^{N_s}\Delta J_0^{(s)}$.

CoX	m_i (μ_B)				$\Delta J_0^{(s)}$ (mRy)				ΔJ_{av}
X	0	1	2	3	0	1	2	3	
Co	1.63	1.63	1.63	1.63	0	0	0	0	0
Pt	0.39	1.67	1.66	1.67	−13	−0.6	−0.8	0.3	−0.4
Ru	0.48	1.58	1.59	1.67	−14	−3.5	−3	−0.1	−1.6
Cr	−2.2	1.45	1.47	1.6	−0.7	−2.8	−2.5	−1	−1.4

The exchange stiffness in magnetic materials is calculated by adding all exchange interactions between magnetic atoms in the crystal. The trends in A_{ex} can be qualitatively understood from the change in the magnetic moments as a result of the alloying. The small moment attributed to the Ru atom combined with the reduction in the moment of its Co neighbors in the $i = 1$ and 2 shells amounts to a significant decrease in the overall exchange coupling constant. While Cr reduces the Co neighboring moments more than Ru, this is mitigated by the very large moment on the Cr atom which acts to increase the exchange constant. Pt in CoPt has a very small moment; however, Pt increases the moment of the Co neighbors and therefore affects A_{ex} the least. The measured trends match this qualitative conclusion.

The prediction of the DFT calculations are also in good agreement with other element-resolved studies of the magnetic moment in Co alloys (CoCr [38,39], CoRu [38,40], and CoPt [41,42]).

D. A_{ex} of Co films obtained using Brillouin scattering

In a conducting film in which the optical skin depth is small compared to the wavelength of light in the free space, the components of the wave vectors of scattered and incident light normal to the film plane are not well defined. For this reason, only momentum components of scattered, k_s, and incident, k_i, wave vectors parallel to the sample surface are conserved in the scattering process, and selection rules are

$$q_\parallel = k_s \sin\theta_s - k_i \sin\theta_i, \quad \Omega = \omega_s - \omega_i, \tag{7}$$

where $q_\parallel$ is the projection of the magnon wave vector parallel to the sample surface, θ_s and θ_i are the angles between the film normal and scattered and incident light, and ω_s and ω_i are angular frequencies of the scattered and incident light, respectively. In our experiment we used the green line from an argon ion laser, $\lambda = 514.5$ nm, and the Brillouin light scattering (BLS) data were collected in the backscattering geometry so that $\theta_s \approx \theta_i = 45^\circ$.

For a homogeneous thin film with a magnetic field H_0 applied perpendicular to the scattering plane and parallel to the film plane, the circularly polarized surface magnon dispersion

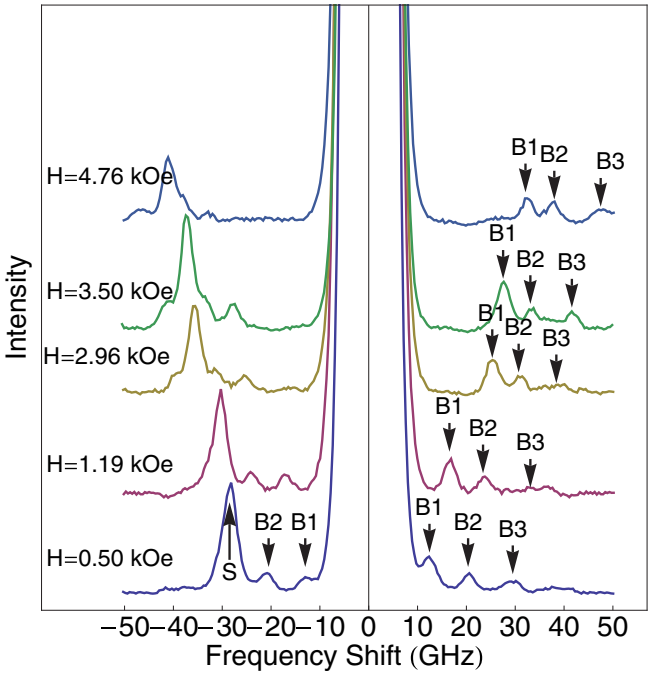

FIG. 8. (Color online) Frequency shift of the standing wave modes as a function of the applied magnetic field.

relation is given by [43]

$$\omega_s = \sqrt{\omega_H(\omega_H + \omega_m) + \frac{\omega_m^2}{4}}, \tag{8}$$

where $\omega_H = \gamma H_0$, $\omega_m = \gamma 4\pi M_{\rm eff}$, $\gamma = g\mu_B/\hbar$ is the gyromagnetic ratio, g is the electron g factor, and μ_B is the Bohr magneton. The effective magnetization in our films can be calculated from the relation $4\pi M_{\rm eff} = 4\pi M_s + 2K_\parallel/M_s - 2K_u/M_s$, where M_s is the film saturation magnetization, $K_\parallel$ is the magnetic anisotropy parallel to the film surface, and K_u is the uniaxial magnetic anisotropy perpendicular to the surface of the film. The Co film studied with BLS is polycrystalline with random in-plane orientation of the grains, and only weak texture of the [0001] direction along the direction perpendicular to the film surface. For this reason $K_\parallel = 0$ and K_u is very small, so we will assume $4\pi M_{\rm eff} = 4\pi M_s$. Then the surface magnon dispersion relation Eq. (8) can be written as

$$\omega_s = \gamma(H_0 + 2\pi M_s), \tag{9}$$

and the bulk magnon dispersion relation is given by [5,44]

$$\omega_b = \gamma\sqrt{\left(H_0 + \frac{2A_{\rm ex}}{M_s}q^2\right)\left(H_0 + 4\pi M_s + \frac{2A_{\rm ex}}{M_s}q^2\right)}, \tag{10}$$

where $\vec{q}$ is the magnon wave vector, $q^2 = q_\parallel^2 + q_\perp^2$. In the films $q_\perp$ can take only discrete values, $q_\perp = n\pi/L$, where L is the sample thickness and $n = 0,1,2,\ldots$.

Figure 8 shows Brillouin scattering spectra of the scattered intensity as a function of frequency shift for an 80 nm Co film for applied external magnetic fields $H_0 = 0.50$, 1.19, 2.96, 3.50, and 4.76 kOe. The peak labeled S that is shifted from -28 GHz for $H_0 = 0.5$ kOe to -41 GHz for $H_0 = 4.76$ kOe

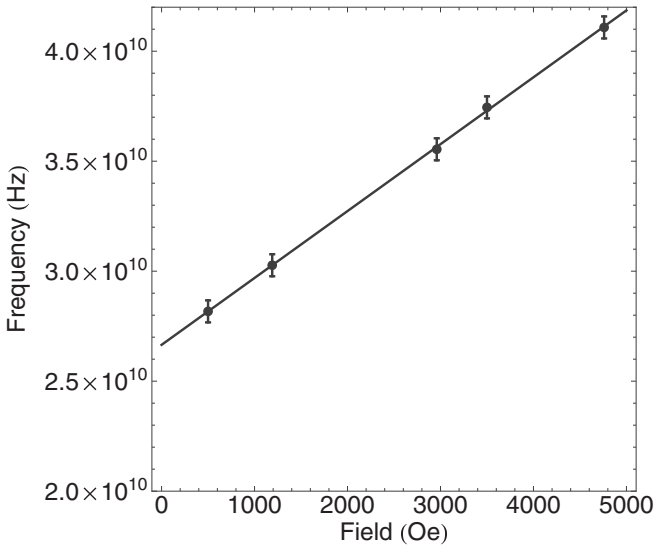

FIG. 9. Surface magnon frequency shift and the fit through the data $g = 2.17$ and $M_s = 1390 \pm 20$ emu/cm^3.

on the left side of the spectrum is the surface magnon. The other resolved peaks at both positive and negative frequency shifts are bulk scattering wave modes $n = 1$, 2, 3.

Figure 9 shows the frequency shift as a function of applied field dependence for the surface magnon. The solid line is a least-squares fit of Eq. (9) to the measured data. The best fit was obtained for $g = 2.17$ and $M_s = 1390 \pm 20$ emu/cm^3. The g and M_s values obtained by fitting are close to that measured for 100 nm Co films with BLS [5].

In Fig. 10 we present frequency shifts as a function of the applied field for the bulk standing spin-wave modes $n = 1$, 2, 3. The solid lines represent least-squares fits of Eq. (10) to the measured data. The best fit was obtained for $M_s = 1330 \pm 40$ emu/cm^3 and $A_{\rm ex} = 1.92 \pm 0.07 \times 10^{-6}$ erg/cm. As expected, M_s values (1390 and 1330 emu/cm^3) obtained from fitting BLS data are practically the same as M_s of

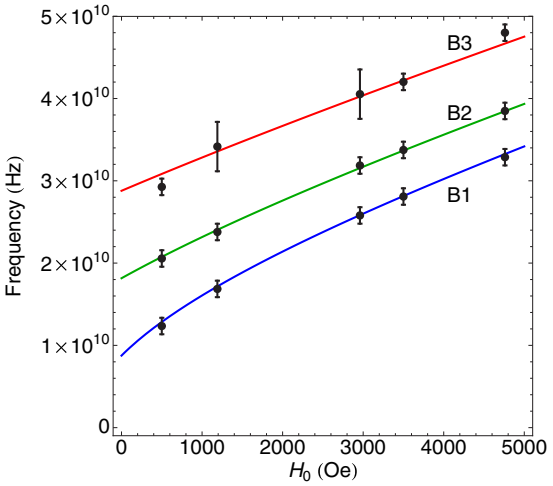

FIG. 10. (Color online) Frequency shift of the three bulk magnon modes (B1, B2, and B3) and a fit through the data. $A_{\rm ex} = 1.9 \times 10^{-6}$ erg/cm and $M_s = 1330 \pm 40$emu/cm^3.

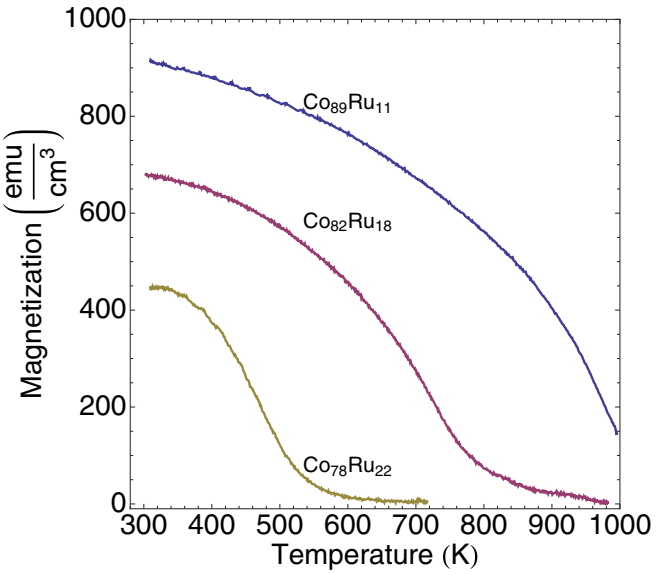

FIG. 11. (Color online) Magnetization versus temperature for three CoRu alloy films. The determined Curie temperatures are $T_c(Co_{89}Ru_{11}) \approx 1035$ K, $T_c(_{Co}83_{Ru}17) = 795$ K, and $T_c(Co_{78}Ru_{22}) = 530$ K.

Ru/Co(80 nm)/Ru that we measured with SQUID. A_{ex} is similar to that measured by Vernon et al. [5]. The A_{ex} values obtained with Brillouin scattering are about 25% larger than the values obtained with the single-layer model, but very close to $A_{ex\,bulk}$ values calculated with the triple-layer model ($A_{ex\,bulk} = 1.79 \times 10^{-6}$ erg/cm) assuming 30% reduction of A_{ex} within 1.2 nm of the spacer layer interface ($A_{ex\,int} = 1.1 \times 10^{-6}$ erg/cm). The discrepancy between the BLS measurement and the results of the single-layer model can thus be attributed to a softening of the magnetic properties at the Co/Ru interfaces. The softening at the Co/Ru interface is expected since adding Ru to Co results in a strong reduction of A_{ex} of Co (Fig. 5). It is also in agreement with results showing the decrease of M_s and A_{ex} of Co films with reducing Co film thickness, t_1, in Ru/Co(t_1)/Ru/Co(t_1)/Ru structures (Fig. 4). This could mean that the single layer is sufficient to determine the mean A_{ex} of a thin film, but the triple-layer model has to be used to extract the bulk value. Unfortunately, the triple-layer model can only be used if the thickness, $M_{s\,int}$, and $A_{ex\,int}$ of the Co interface layers facing a Ru spacer layer are known. Otherwise, the best fit from the triple-layer model is achieved for $A_{ex\,int} \approx A_{ex\,bulk} \approx A_{ex\,ext}$ (Table II).

E. Curie temperature measurements of CoRu

The Curie temperature, T_c, is proportional to the mean exchange coupling between atoms and therefore to A_{ex} [45]. For this reason, we have summarized the T_c data available in the literature for all the investigated CoX alloys in Table I. We have also measured T_c of $Co_{100-\delta}Ru_\delta$ ($\delta = 11, 17, 22$). The $M(T)$ data are presented in Fig. 11. As was observed from fitting $M(H)$ data of CoX/Ru/CoX and the DFT calculations, the addition of Ru and Cr to Co reduces A_{ex} the most. This is also evident from Table I as these two elements reduce T_c the most. Our T_c measurements for CoRu are between those obtained for hcp and fcc CoRu. The investigated films should mostly have hcp crystal structure. However, the presence of stacking faults may be present affecting both A_{ex} and T_c of investigated films [35]. From Fig. 11, T_c of $Co_{89}Ru_{11}$ is about 1035 K, of $Co_{83}Ru_{17}$ is 795 K, and of $Co_{78}Ru_{22}$ is 530 K. Since T_c of pure Co, T_c(Co), is 1440 K [1] adding 11, 17, and 22 at. % of Ru reduces T_c to 0.72 T_c(Co), 0.55 T_c(Co) and 0.37 T_c(Co), respectively.

T_c measurements were performed on four times thicker CoRu films (40 nm) than A_{ex} measurements (10 nm). Thus, T_c measurements mostly reflect the bulk CoRu magnetic properties. On the other hand, BLS and SQUID magnetic measurements indicate that the interface contributions in 10 nm CoRu films used for A_{ex} measurements cannot be neglected. This could in part explain a slower rate of decrease of T_c in 40 nm CoRu films than A_{ex} in 10 nm CoRu with Ru concentration. First-principles calculations also showed that the rate of change of A_{ex} of CoRu with Ru concentration is faster than the measured rate of decrease of T_c. In both our experimental measurements and calculations we determine A_{ex} along the [0001] direction (by inducing a spin spiral to the moments perpendicular to the [0001] crystal direction). On the other hand, the change in T_c is proportional to the mean change of A_{ex} in CoRu films. This may also contribute to the observed discrepancy.

VI. CONCLUSION

We have shown that A_{ex} of FM films can be determined by fitting the $M(H)$ dependence of a FM/NM/FM film structure, in which the FMs are antiferromagnetically coupled across the NM spacer layer, to a one-dimensional micromagnetic model. In single-crystal and textured films this method allows for the measurement of A_{ex} along a particular crystallographic direction. This eliminates uncertainty in A_{ex} measurements due to the dependance of A_{ex} on the crystal orientation. Singh *et al.* showed that in the hcp Co lattice A_{ex} calculated by inducing a spin spiral to the moments perpendicular to the [0001] and [11-20] crystal directions differ almost 30% [23].

This method was used to infer A_{ex} for Co films with thickness ranging from 2.4 to 20 nm, and for 10-nm-thick CoX alloy layers (X = Cr, Fe, Ni, Ru, Pd, and Pt) along the [0001] direction of CoX hcp structure. We have tested two micromagnetic models: the *single-layer model*, in which A_{ex} is kept constant across magnetic layers, and the *three-layer model*, in which A_{ex} was allowed to vary at the interfaces with neighboring nonmagnetic layers. We have also tested the single-layer model assuming that the antiferromagnetic coupling (AFC) between magnetic layers is described by a bilinear term, and by both bilinear and biquadratic terms. From comparing the quality of fits we conclude that for magnetic layers with thickness exceeding 6 nm the magnetization reversal in Co/Ru/Co and CoX/Ru/CoX can be described using the single-layer model and assuming that AFC in the model is described by the bilinear term only. The quality of the fit of $M(H)$ data of Co(10 nm)/Ru/Co(10 nm) achieved with the single-layer and three-layer models is the same. So we decided to use the single-layer model in order to minimize the number of free parameters. For thinner Co and CoX layers, AFC in the single-layer model has to include both the bilinear and

biquadratic terms. This is expected since the biquadratic term is inversely proportional to square of the magnetic film thickness.

The dependence A_{ex} and M_s on thickness of a Co layer was obtained from fitting $M(H)$ data of Co(t_1)/Ru/Co(t_1) structures, where t_1 ranged from 2.4 nm to 20 nm. The results indicate that both M_s and A_{ex} increase with t_1: the increase is steep for $t_1 < 3$ nm (for M_s) and for $t_1 < 6$ nm (for A_{ex}), and gradual for thicker Co layers. The effect of alloying on M_s and A_{ex} of Co was obtained by fitting the $M(H)$ dependence of CoX(10 nm)/Ru/CoX(10 nm) (X = Cr, Fe, Ni, Ru, Pd, and Pt). The results show that A_{ex} of Co alloys does not necessarily scale with M_s; A_{ex} approximately decreases at the rate of 3.7%, 4.7%, 2.1%, 1.3%, and 1.8%, while M_s decreases at the rate of 3.6%, 2.7%, 1.0%, 1.0%, and 0.4% per addition of 1 at. % of Cr, Ru, Pd, Pt, and Ni. Addition of Fe does not change A_{ex} of Co and increases M_s of Co approximately 0.8% per addition of 1 at. % of Fe.

We also measured J_{RKKY} versus M_s^2 of CoX in CoX/Ru/CoX. For a constant Ru spacer layer thickness, J_{RKKY} is linearly dependent on M_s^2, as predicted by the mean-field theory calculations [38].

The dependence of A_{ex} on dopant content δ was calculated from first-principles calculations assuming uniform dopant atoms distribution and the dilute concentration limit where the exchange coupling between the dopant atoms is negligible. The A_{ex} trends obtained from the single-layer model for CoX (X = Cr, Ru, and Pt) are in agreement with the trends obtained from first-principles calculations. The calculations on CoX show that the substituted Cr atoms are antiferromagnetically coupled to the Co neighbors and have a very large magnetic moment of $-2.2\ \mu_B$. The substituted Pt and Ru atoms coupled ferromagnetically to the Co atoms and their induced magnetic moments are 0.39 μ_B for Pt and 0.48 μ_B for Ru. The first-principles calculations also show that the addition of Cr and Ru atoms reduces the magnetic moment of the surrounding Co atoms while the addition of Pt slightly increases the neighboring Co moments. The trends in A_{ex} can be qualitatively understood from the change in the magnetic moments as a result of the alloying. The small moment attributed to the Ru atom combined with the reduction in the moment of its Co neighbors amounts to a significant decrease in the overall A_{ex}. While Cr reduces the neighboring moments more than Ru, this is mitigated by the very large moment on the Cr atom, which acts to increase A_{ex}. Pt in CoPt has a very small moment. However, Pt increases the moment of its Co neighbors and therefore affects A_{ex} the least. The measured trends match this qualitative conclusion.

A_{ex} of 10 nm Co layers obtained by fitting $M(H)$ of Co/Ru/Co with the single-layer model is about 20% lower than the Brillouin scattering results on thicker Co films. We also observed slower rate of decrease of T_c in thicker CoRu films than A_{ex} in thinner CoRu with Ru concentration. These results suggest that A_{ex} of Co at the interfaces with nonmagnetic Ru layers is reduced. This is expected since Ru is very efficient in reducing A_{ex} of Co. It is also in agreement with results showing the decrease of M_s and A_{ex} of Co films with reducing Co film thickness, t_1, in Ru/Co(t_1)/Ru/Co(t_1)/Ru structures. To account for reduction of A_{ex} and M_s at the Co/Ru interface we used the single-layer model to measure A_{ex} and M_s of a 12-atomic-layer-thick Co layer in Ru/Co(24 Å)/Ru/Co(24 Å)/Ru. These results were then used in the triple-layer model to estimate the A_{ex} of bulk Co. The A_{ex} values obtained using this procedure are in a good agreement with those we obtained with Brillouin light scattering.

[1] J. M. D. Coey, *Magnetism and Magnetic Materials* (Cambridge University Press, Cambridge, 2009).
[2] R. Victora, IEEE Trans. Magn. **41**, 537 (2005).
[3] D. Suess, T. Schrefl, S. Fähler, M. Kirschner, G. Hrkac, F. Dorfbauer, and J. Fidler, Appl. Phys. Lett. **87**, 012504 (2005).
[4] E. Girt, A. Y. Dobin, B. Valcu, H. J. Richter, X. Wu, and T. P. Nolan, IEEE Trans. Magn. **43**, 2166 (2007).
[5] S. P. Vernon, S. M. Lindsay, and M. B. Stearns, Phys. Rev. B **29**, 4439 (1984).
[6] A. Yoshihara, Y. Haneda, Y. Shimada, and T. Fujimura, J. Appl. Phys. **66**, 328 (1989).
[7] X. Liu, R. Sooryakumar, C. J. Gutierrez, and G. A. Prinz, J. Appl. Phys. **75**, 7021 (1994).
[8] X. Liu, M. M. Steiner, R. Sooryakumar, G. A. Prinz, R. F. C. Farrow, and G. Harp, Phys. Rev. B **53**, 12166 (1996).
[9] H. A. Alperin, J. Appl. Phys. **37**, 1052 (1966).
[10] A. Michels, J. Weissmüller, A. Wiedenmann, J. Pedersen, and J. Barker, Philos. Mag. Lett. **80**, 785 (2000).
[11] G. Shirane, J. Appl. Phys. **39**, 383 (1968).
[12] P. Tannenwald and R. Weber, Phys. Rev. **121**, 715 (1961).
[13] P. Talagala, P. S. Fodor, D. Haddad, R. Naik, L. E. Wenger, P. P. Vaishnava, and V. M. Naik, Phys. Rev. B **66**, 144426 (2002).
[14] J. O. Rantschler, C. Alexander, and H.-S. Jung, J. Magn. Magn. Mater. **286**, 262 (2005).
[15] C. Antoniak, J. Lindner, K. Fauth, J.-U. Thiele, J. Minár, S. Mankovsky, H. Ebert, H. Wende, and M. Farle, Phys. Rev. B **82**, 064403 (2010).
[16] A. Scholl, M. Liberati, E. Arenholz, H. Ohldag, and J. Stöhr, Phys. Rev. Lett. **92**, 247201 (2004).
[17] E. Girt, W. Huttema, O. N. Mryasov, E. Montoya, B. Kardasz, C. Eyrich, B. Heinrich, A. Y. Dobin, and O. Karis, J. Appl. Phys. **109**, 07B765 (2011).
[18] C. Eyrich, W. Huttema, M. Arora, E. Montoya, F. Rashidi, C. Burrowes, B. Kardasz, E. Girt, B. Heinrich, O. N. Mryasov, M. From, and O. Karis, J. Appl. Phys. **111**, 07C919 (2012).
[19] O. N. Mryasov, A. J. Freeman, and A. I. Liechtenstein, J. Appl. Phys. **79**, 4805 (1996).
[20] A. I. Liechtenstein, M. I. Katsnelson, and V. A. Gubanov, J. Phys. F: Met. Phys. **14**, L125 (1984).
[21] O. N. Mryasov, J. Magn. Magn. Mater. **272-276**, 800 (2004).
[22] O. N. Mryasov, U. Nowak, K. Y. Guslienko, and R. W. Chantrell, Europhys. Lett. **69**, 805 (2005).
[23] A. Singh, O. Mryasov, S. Gupta, X. Wang, and E. Girt, IEEE Trans. Magn. **48**, 3731 (2012).
[24] O. N. Mryasov, V. A. Gubanov, and A. I. Liechtenstein, Phys. Rev. B **45**, 12330 (1992).
[25] L. Yan and J. A. Woollam, J. Appl. Phys. **92**, 4386 (2002).

[26] S. S. P. Parkin, N. More, and K. P. Roche, Phys. Rev. Lett. **64**, 2304 (1990).
[27] E. Girt and H. Richter, IEEE Trans. Magn. **39**, 2306 (2003).
[28] T. Nishizawa and K. Ishida, Bull. Alloy Phase Diagrams **4**, 390 (1983).
[29] K. Ishida and T. Nishizawa, Bull. Alloy Phase Diagrams **11**, 357 (1990).
[30] H. Okamoto, J. Phase Equilib. Diffus. **29**, 383 (2008).
[31] J. Crangle and D. Parsons, Proc. R. Soc. London, Ser. A **255**, 509 (1960).
[32] H. Sato, T. Shimatsu, Y. Okazaki, O. Kitakami, S. Okamoto, H. Aoi, H. Muraoka, and Y. Nakamura, IEEE Trans. Magn. **43**, 2106 (2007).
[33] K. Ishida and T. Nishizawa, J. Phase Equilib. **12**, 83 (1991).
[34] H. Okamoto, J. Phase Equilib. **22**, 591 (2001).
[35] D. Laughlin and D. Lambeth, IEEE Trans. Magn. **37**, 1456 (2001).
[36] J. Brandenburg, R. Hühne, L. Schultz, and V. Neu, Phys. Rev. B **79**, 054429 (2009).
[37] W. H. Press, S. A. Teukolsky, W. T. Vetterling, and B. P. Flannery, *Numerical Recipes: The Art of Scientific Computing*, 3rd. ed. (Cambridge University Press, Cambridge, 2007).
[38] P. Bruno, J. Phys.: Condens. Matter **11**, 9403 (1999).
[39] K. M. Kemner, Y. U. Idzerda, V. G. Harris, V. Chakarian, W. T. Elam, C.-C. Kao, E. Johnson, Y. C. Feng, D. E. Laughlin, C.-T. Chen, K.-B. Lee, and J. C. Lodder, J. Appl. Phys. **81**, 1002 (1997).
[40] H. Hashizume, K. Ishiji, J. C. Lang, D. Haskel, G. Srajer, J. Minár, and H. Ebert, Phys. Rev. B **73**, 224416 (2006).
[41] F. Menzinger and A. Paoletti, Phys. Rev. **143**, 365 (1966).
[42] P. Poulopoulos, F. Wilhelm, V. Kapaklis, N. Jaouen, M. Angelakeris, A. Rogalev, and C. Politis, Phys. Status Solidi (a) **201**, 3243 (2004).
[43] M. Wu, *Solid State Physics*, Vol. 62 (Elsevier, Inc., Amsterdam, 2011), pp. 163–224.
[44] H. M. Olson, P. Krivosik, K. Srinivasan, and C. E. Patton, J. Appl. Phys. **102**, 023904 (2007).
[45] N. Inaba and M. Futamoto, J. Magn. Magn. Mater. **226-230**, 1014 (2001).